X線多波回折理論の導出と計算機シミュレーションおよび実験による検証

回転型四象限X線移相子システムとピンホールトポグラフ

Rotating four-quadrant phase retarder system and pinhole topographs

Acta Cryst. **A62** (2006) 237-247, Acta Cryst. **A67** (2011) 550-556,
Acta Cryst. **A75** (2019) 474-482,
日本放射光学会誌「放射光」**33** (2020) 61-80 [Invited].

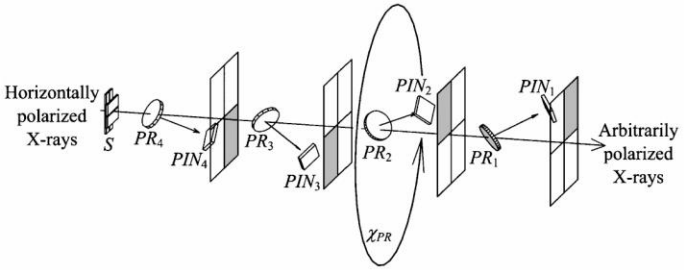

Fig. 4 Schematic drawing of the 'rotating four-quadrant phase retarder system' [reproduction of Fig. 3 in Okitsu *et al.* (2006)[29]].

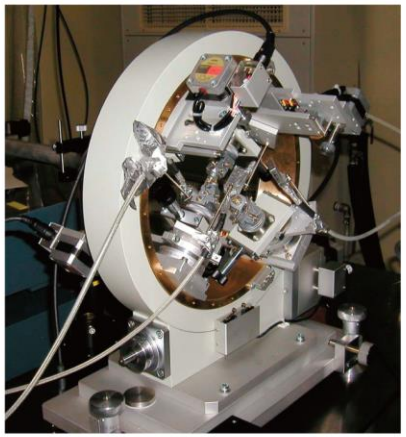

Fig. 5 (Color online) Photograph of the 'rotating four-quadrant phase retarder system' [reproduction of Fig. 3(*b*) in Okitsu *et al.* (2012)[31]].

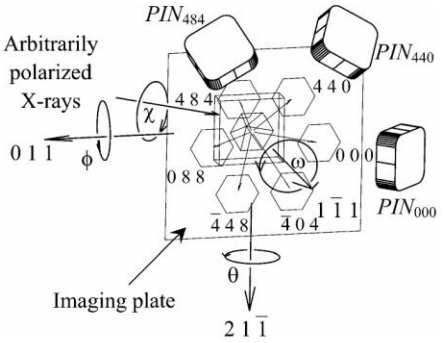

Fig. 6 A schematic drawing of the goniometer on which the sample crystal was mount (reproduction of Fig. 7 in Okitsu *et al.* (2006)[29]).

二象限X線移相子システム

Two-quadrant phase retarder system

J. Synchron Rad. 8 (2001) 33-37.

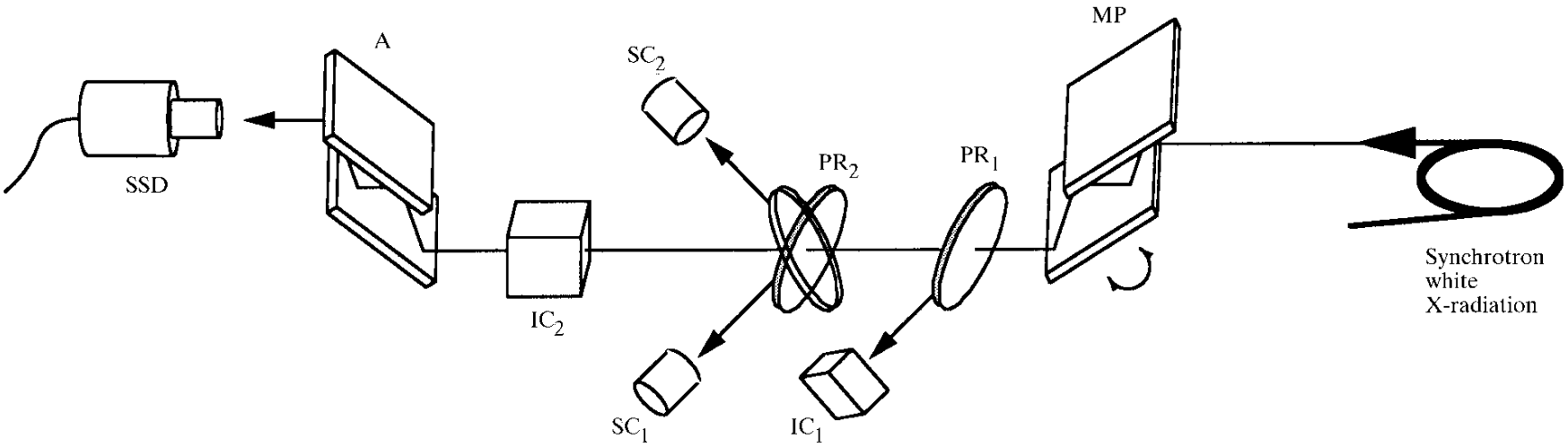

二象限X線移相子システム

Two-quadrant phase retarder system

J. Synchron Rad. 8 (2001) 33-37.

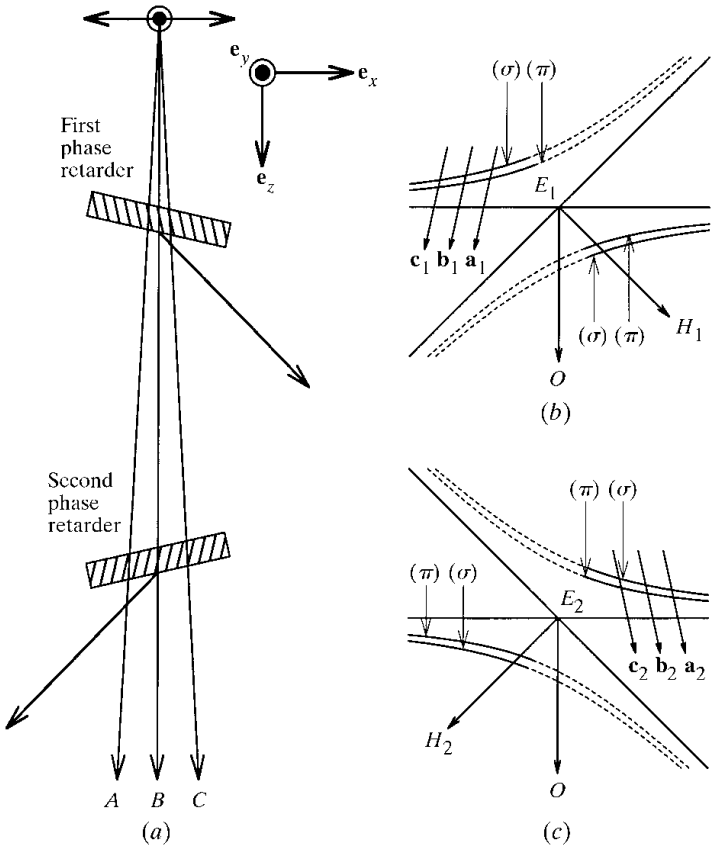

Figure 1
(*a*) Arrangement of the X-ray double phase retarder system to compensate for the off-axis aberration of the transmission-type phase retarder. (*b*), (*c*) Dispersion surfaces in reciprocal space corresponding to the first and second phase retarders, respectively.

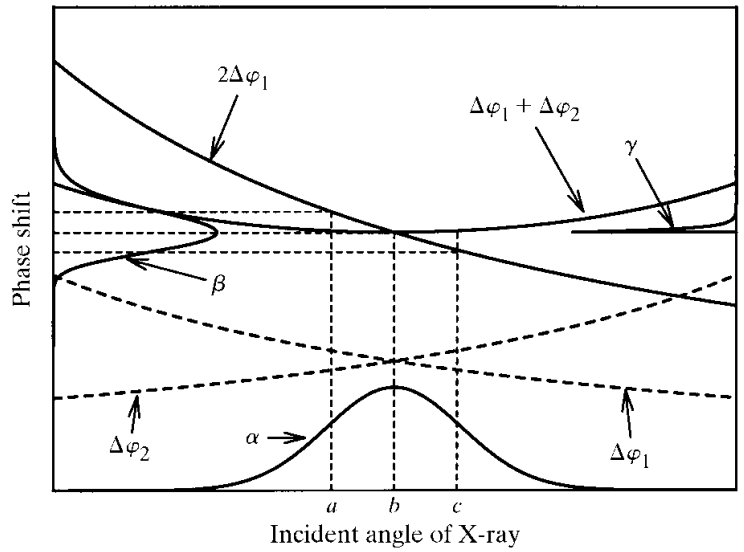

Figure 2
Phase shifts with phase retarders as functions of the incident angle of the X-rays. Phase shifts, $\Delta\varphi_1$ and $\Delta\varphi_2$ given by the first and second phase retarders arranged in the anti-parallel geometry are drawn as dashed curves. Phase shifts given by the double phase retarders (solid curves) arranged in the parallel and anti-parallel geometries are given by $2\Delta\varphi_1$ and by $\Delta\varphi_1 + \Delta\varphi_2$, respectively.

二象限X線移相子システム

Two-quadrant phase retarder system

J. Synchron Rad. 8 (2001) 33-37.

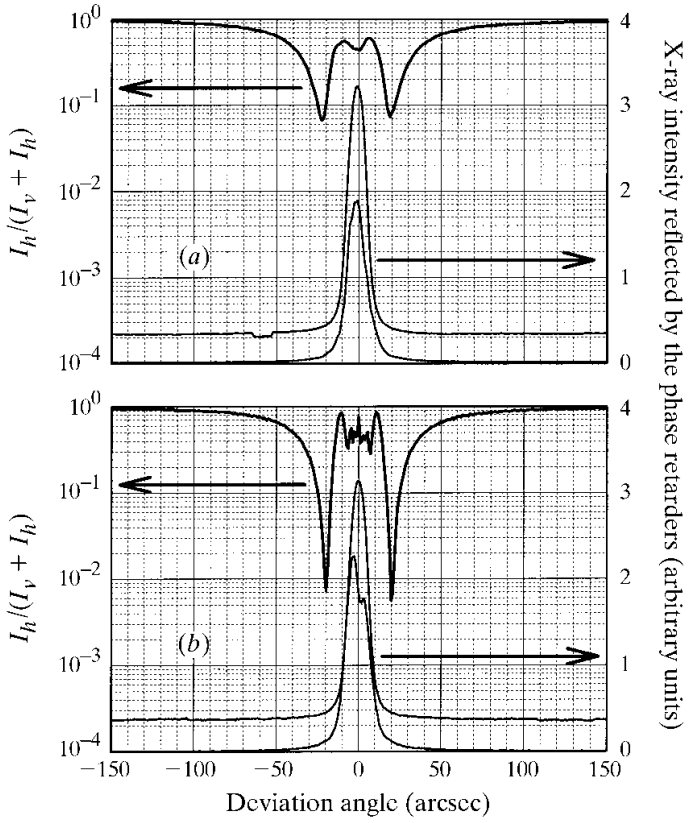

Figure 4
The rate of the horizontally polarized component to the total X-ray intensity (logarithmic left-hand ordinate) as a function of deviation angle from the Bragg condition of the first and second phase retarders. The right-hand ordinate shows intensities of X-rays reflected by the first (upper curve) and the second (lower curve) phase retarders. (*a*) and (*b*) correspond to cases of parallel and anti-parallel geometries, respectively.

四象限X線移相子システム

Four-quadrant phase retarder system

Acta Cryst. **A58** (2002) 146-154.

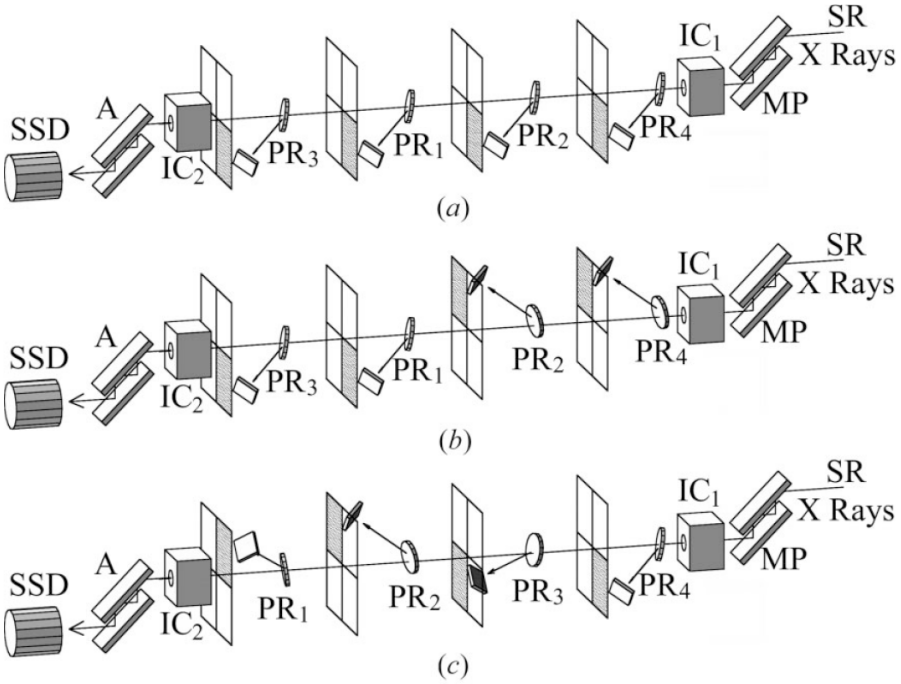

Figure 7
Experimental arrangements of quadruple phase retarders in (*a*) single (one-quadrant), (*b*) double (two-quadrant) and (*c*) four-quadrant geometries. MP: a silicon channel-cut monochromatizing-polarizer equipped with Hart–Rodrigues's offset mechanism giving four-bounced 422 reflection in a symmetric Bragg geometry. *A*: an analyzer crystal similar to the polarizer. PR_1, PR_2, PR_3 and PR_4: diamond (100)-oriented phase-retarder crystals giving 111 reflection in an asymmetric Laue geometry whose thicknesses are 318, 314, 301 and 313 μm, respectively. IC_1 and IC_2: ionization chambers. SSD: a solid-state detector of germanium. Reflected X-rays from the four phase retarders are monitored by four PIN photodiodes.

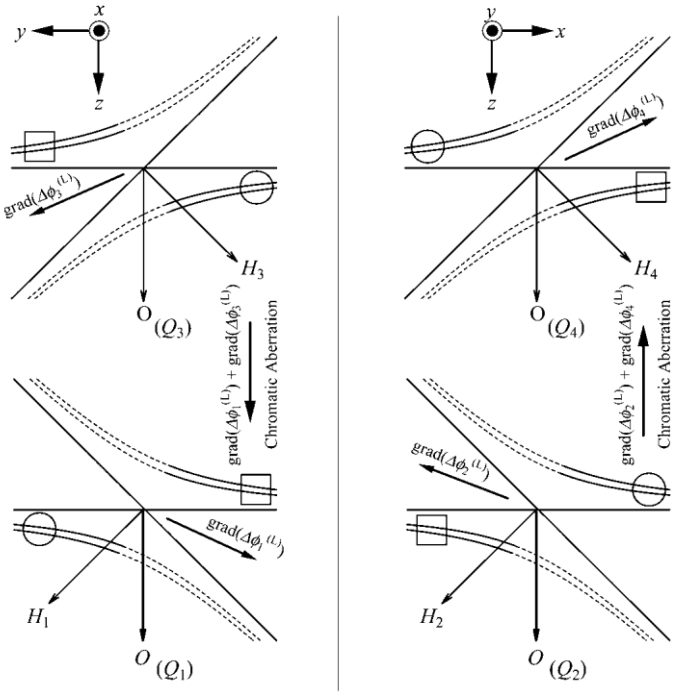

Figure 6
Four dispersion surfaces of a four-quadrant phase-retarder system. These figures clarify the three-dimensional Fig. 5 by drawing dispersion surfaces of odd-numbered-quadrant phase retarders on the left and those of even-numbered-quadrant phase retarders on the right. Suffix n ($n \in \{1, 2, 3, 4\}$) in Q_n, H_n and $\Delta\phi_n^{(L)}$ corresponds to an nth-quadrant phase retarder. The planes of the drawings are rotated by 90° around the direction of vector **z** (direction of transmitted X-ray propagation) between left- and right-hand drawings. It can be understood that directions of chromatic aberrations due to odd-numbered-quadrant and even-numbered-quadrant phase retarders are contrary and then cancelled out with each other. A left-screwed polarization ($\pi > \sum_{n=1}^{4} \phi_n^{(L)} > 0$) is generated by using angular regions indicated by four circles. On the other hand, a right-screwed polarization ($0 > \sum_{n=1}^{4} \phi_n^{(L)} > -\pi$) is generated at regions indicated by four squares.

四象限X線移相子システム

Four-quadrant phase retarder system

- 日本放射光学会誌「放射光」16 (2003) 236-244.

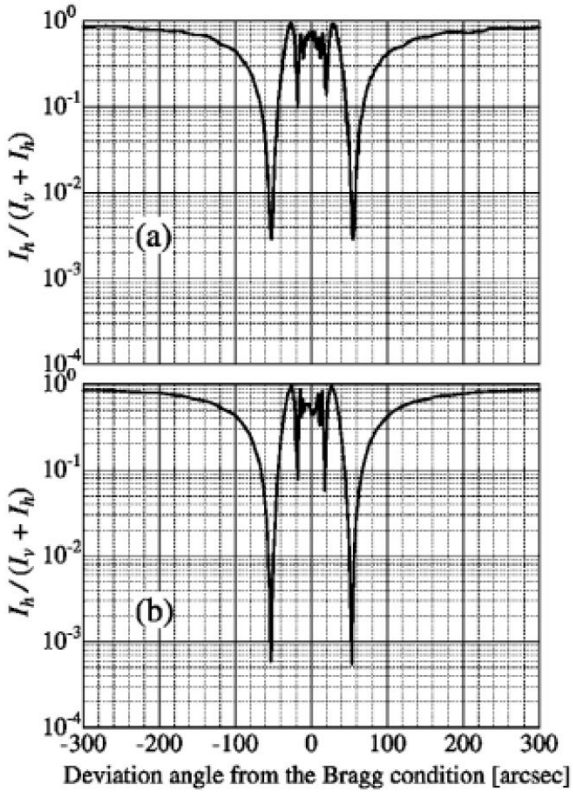

Figure 7. Rate of residual horizontal-polarized component of X-rays whose polarization state was converted from the horizontal polarization by the four-quadrant phase retarder system measured at station BL−15C of the Photon Factory whose distance from radiation source is farther than station BL−4A[47]. (a) corresponds to Fig. 6(c) measured at BL−4A and then to the geometry shown in Fig. 5 (c). (b) was measured with a (+ − + −, − + − +) geometry of parallel nicol polarizer and analyzer in which energy spread of X-rays was suppressed into 0.05 eV.

回転型四象限X線移相子システムとピンホールトポグラフ

Rotating four-quadrant phase retarder system and pinhole topographs

Acta Cryst. **A62** (2006) 237-247, Acta Cryst. **A67** (2011) 550-556,
Acta Cryst. **A75** (2019) 474-482,
日本放射光学会誌「放射光」**33** (2020) 61-80 [Invited].

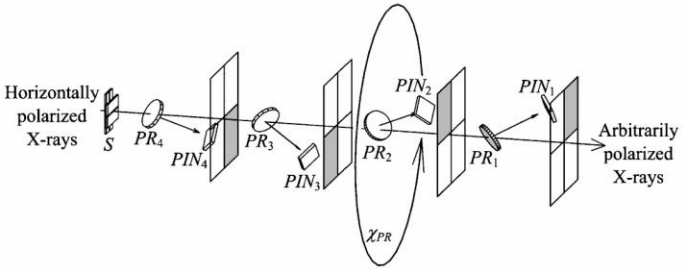

Fig. 4 Schematic drawing of the 'rotating four-quadrant phase retarder system' [reproduction of Fig. 3 in Okitsu *et al.* (2006)[29]].

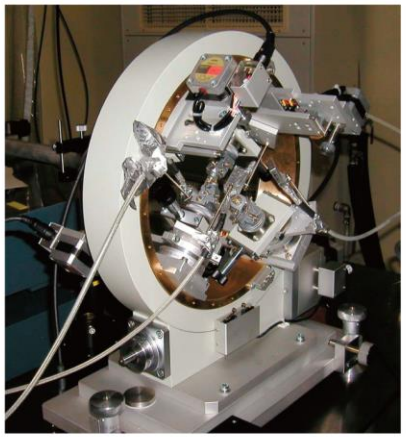

Fig. 5 (Color online) Photograph of the 'rotating four-quadrant phase retarder system' [reproduction of Fig. 3(*b*) in Okitsu *et al.* (2012)[31]].

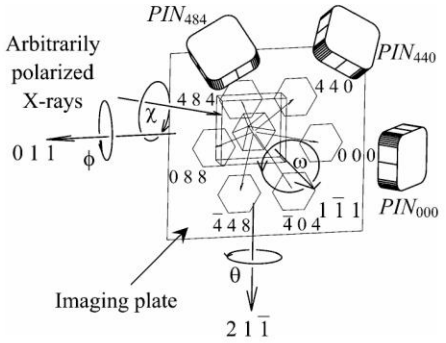

Fig. 6 A schematic drawing of the goniometer on which the sample crystal was mount (reproduction of Fig. 7 in Okitsu *et al.* (2006)[29]).

Experiment and computer simulation for three-beam case (18.245 keV)

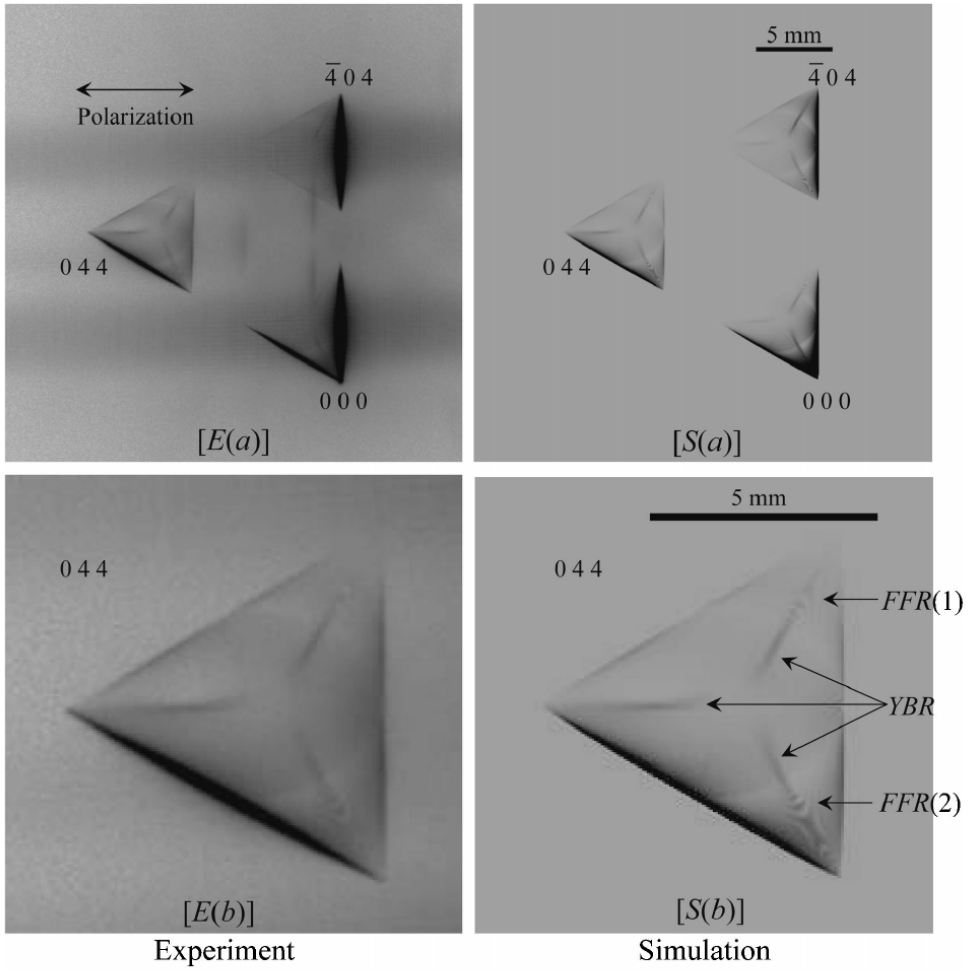

Fig. 7 [$E(a)$] and [$S(a)$] are experimentally obtained and computer-simulated three-beam X-ray pinhole topographs with an incidence of horizontal-linearly polarized X-rays whose photon energy was 18.245 keV. [$E(b)$] and [$S(b)$] are 0 4 4 reflected X-ray images enlarged from [$E(a)$] and [$S(a)$], respectively [reproduction of Fig. 5 in Okitsu *et al.* (2012)[31]].

Experiment and computer simulation for four-beam case (18.245 keV)

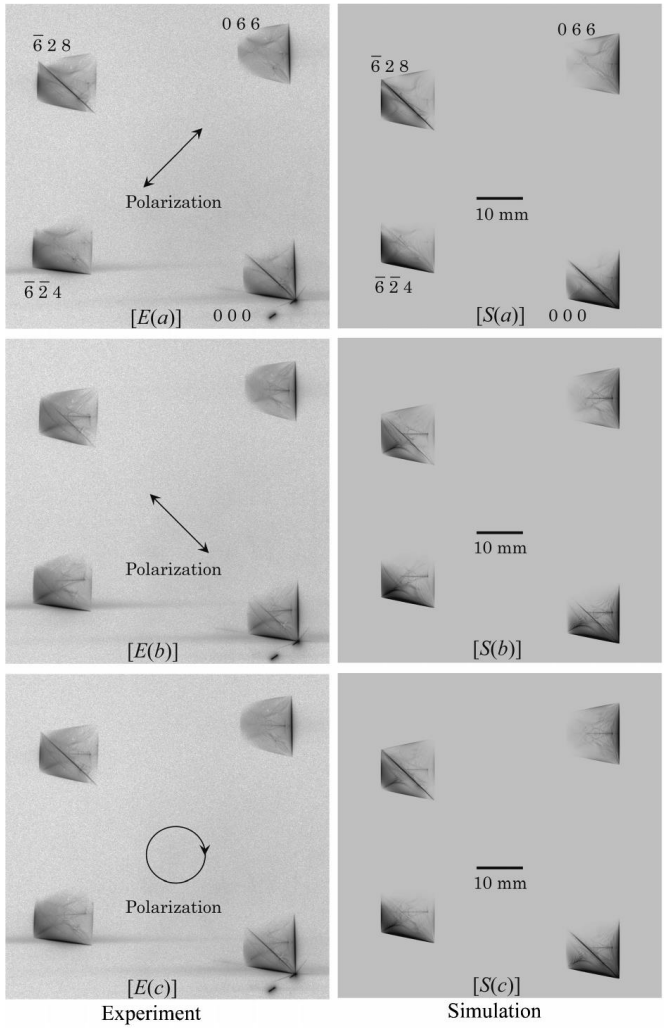

Fig. 8 [$E(x)$] and [$S(x)$] ($x \in \{a, b, c\}$) are experimentally obtained and computer-simulated four-beam X-ray pinhole topographs with an incidence of $+45°$-inclined-linearly, $-45°$-inclined-linearly and right-screwed-circularly polarized X-rays whose photon energy was 18.245 keV [reproduction of Fig. 6 in Okitsu *et al.* (2012)[31]].

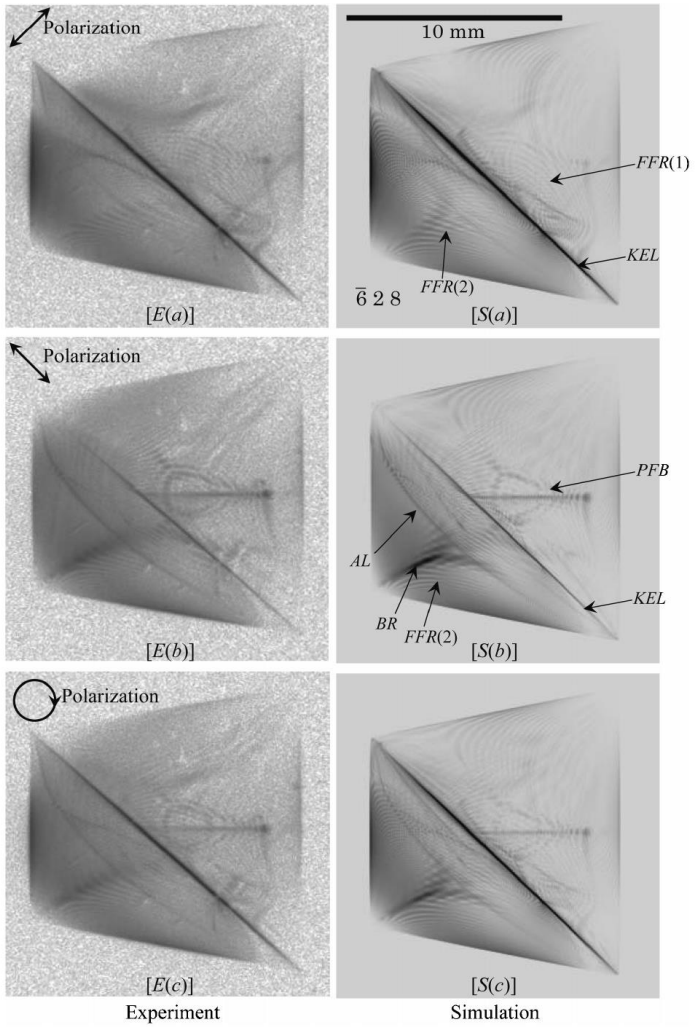

Fig. 9 [$E(x)$] and [$S(x)$] ($x \in \{a, b, c\}$) are enlargements of $\bar{6}$ 2 8 reflected X-ray images in Fig. 8 [$E(x)$] and [$S(x)$] [reproduction of Fig. 7 in Okitsu *et al.* (2012)[31]].

Experiment and computer simulation for five-beam case (18.245 keV)

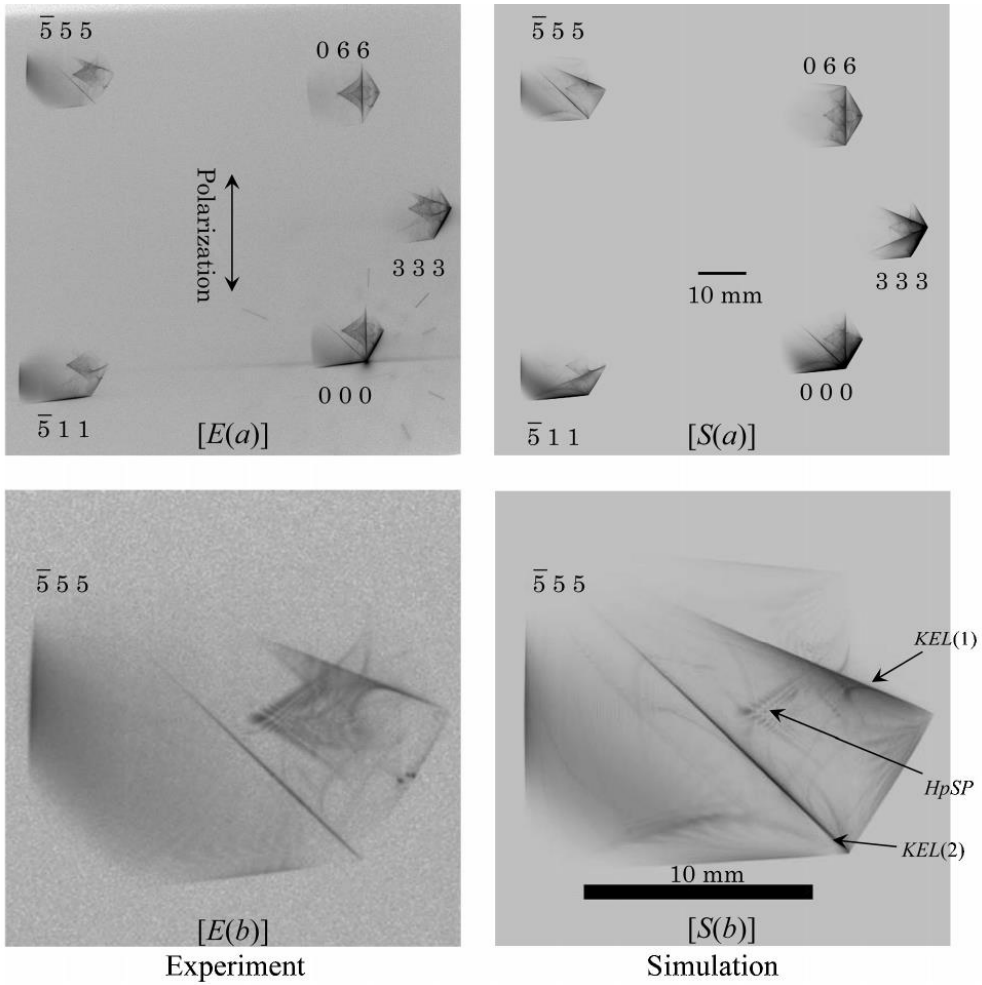

Fig. 11 [$E(a)$] and [$S(a)$] are experimentally obtained and computer-simulated five-beam X-ray pinhole topographs with an incidence of vertical-linearly polarized X-rays whose photon energy was 18.245 keV. [$E(b)$] and [$S(b)$] are $\bar{5}$ 5 5 reflected X-ray images enlarged from [$E(a)$] and [$S(a)$] [reproduction of Fig. 8 in Okitsu *et al.* (2012)[31]].

Experiment and computer simulation for six-beam case (18.245 keV)

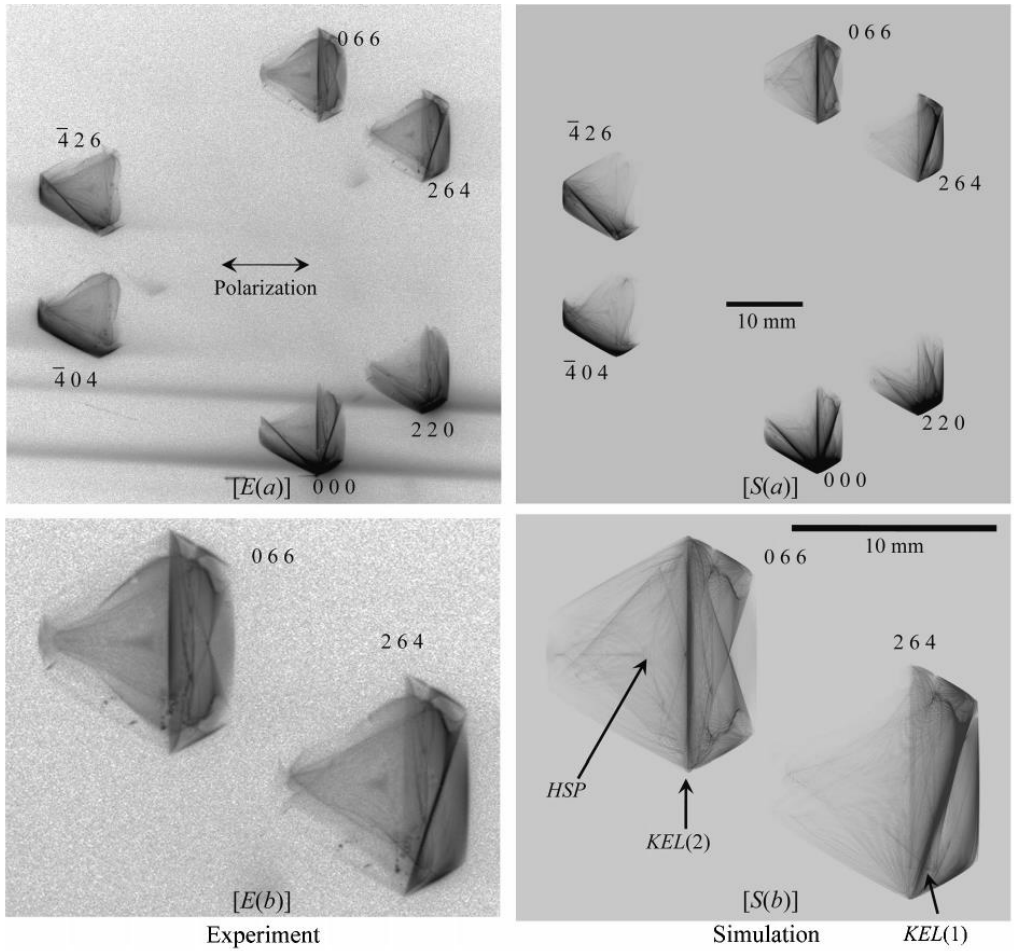

Fig. 12 $[E(a)]$ and $[S(a)]$ are experimentally obtained and computer-simulated six-beam X-ray pinhole topographs with an incidence of horizontal-linearly polarized X-rays with a photon energy of 18.245 keV. $[E(b)]$ and $[S(b)]$ are 0 6 6 and 2 6 4 reflected X-ray images enlarged from $[E(a)]$ and $[S(a)]$ [reproduction of Fig. 9 in Okitsu *et al.* (2012)[31]].

Experimental and computer-simulated topographs

six-beam case for a channel-cut silicon crystal (18.475 keV)

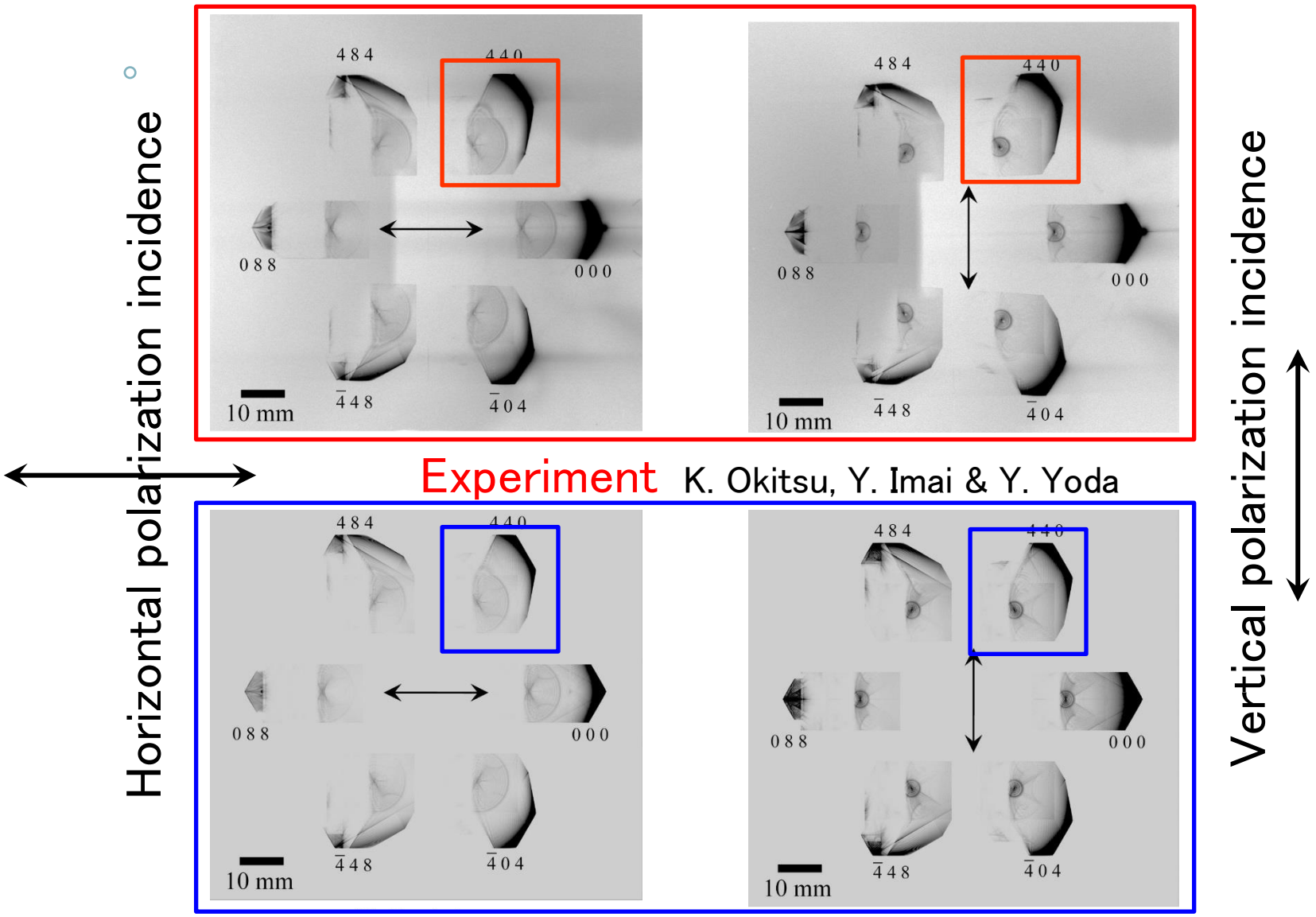

Experimentally obtained topographs and computer simulations

Six-beam case　Chennel-cut crystal　(Enlarged)

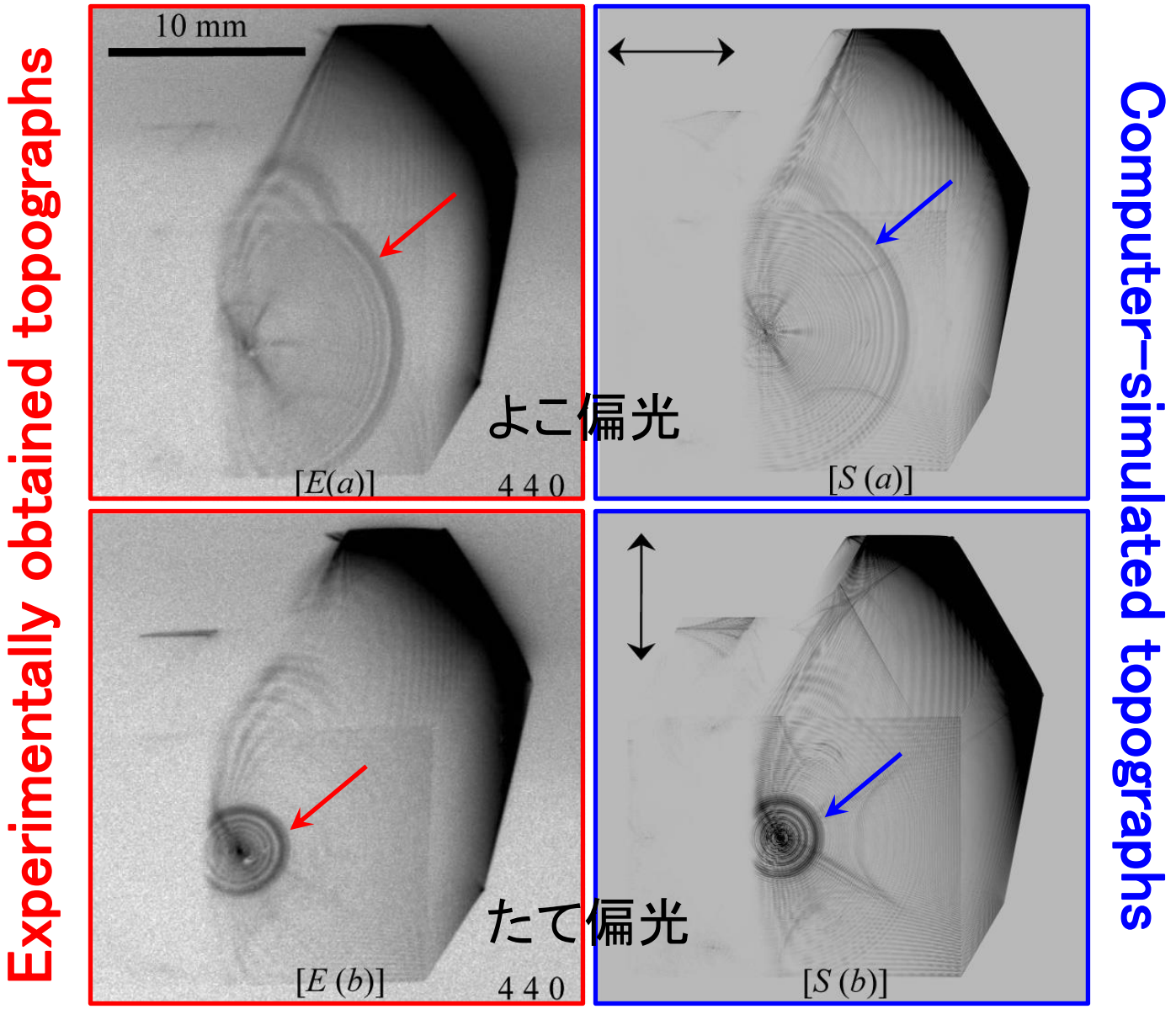

Experiment and computer simulation for eight-beam case (18.245 keV)

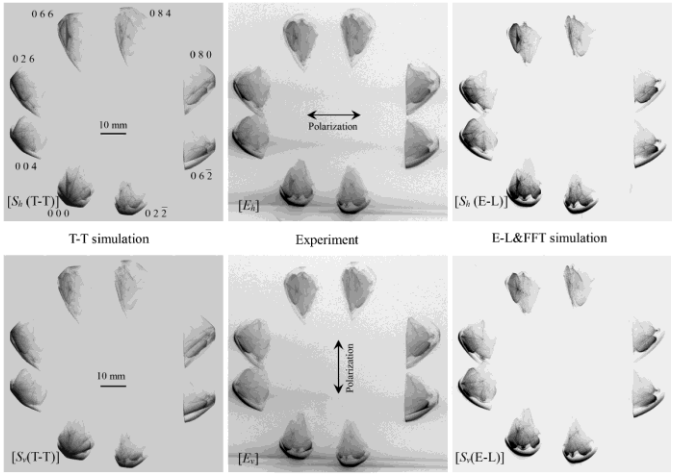

Fig. 13 [S_x(T–T)], [E_x], and [S_x(E–L)] ($x \in \{h, v\}$) are the T–T simulated, experimentally obtained and E-L&FFT simulated eight-beam pinhole topographs for horizontally ($x = h$) and vertically ($x = v$) polarized incident X-rays [reproduction of Fig. 5 in Okitsu *et al.* (2019)[39]].

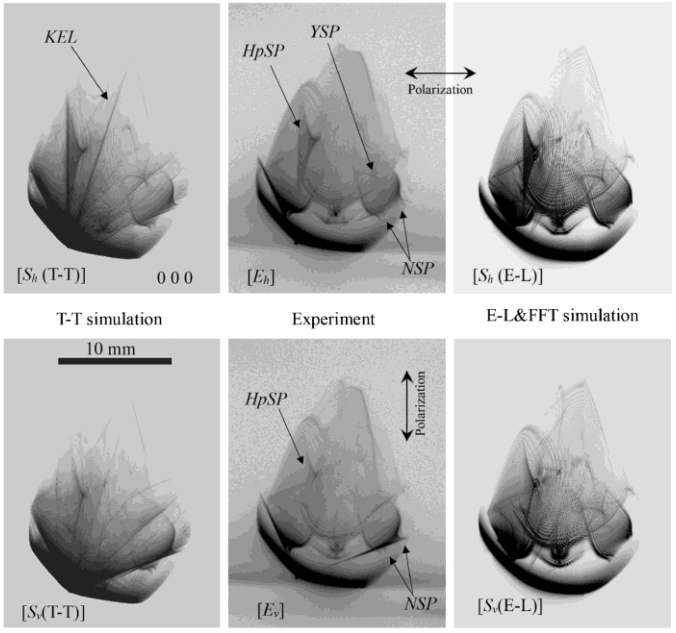

Fig. 14 Enlargements of the 0 0 0 forward-diffracted images in Fig. 13 [reproduction of Fig. 6 in Okitsu *et al.* (2019)[39]].

Experiment and computer simulation for twelve-beam case (22.0 keV)

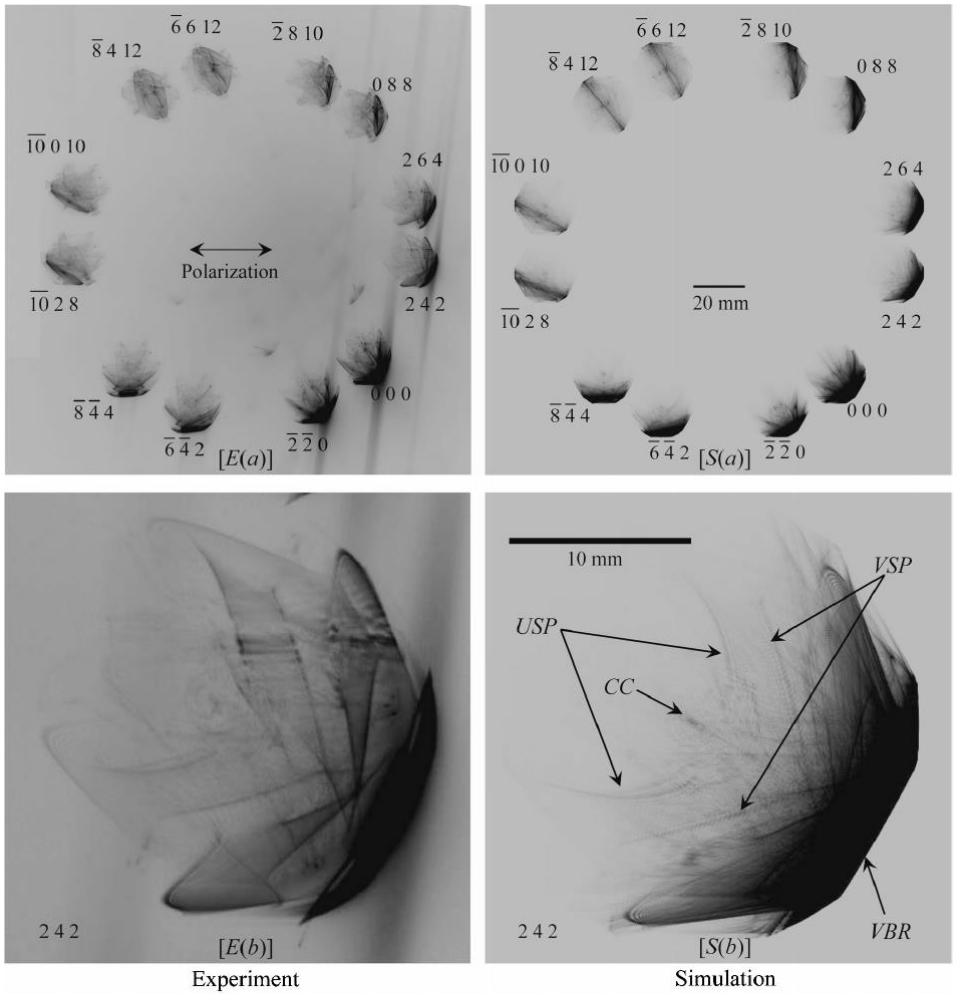

Fig. 17 $[E(a)]$ and $[S(a)]$ are experimentally obtained and computer-simulated twelve-beam X-ray pinhole topographs with an incidence of horizontal-linearly polarized X-rays whose photon energy was 22.0 keV. $[E(b)]$ and $[S(b)]$ are 2 4 2 reflected X-ray images enlarged from $[E(a)]$ and $[S(a)]$ [reproduction of Fig. 12 in Okitsu *et al.* (2012)[31]].

Experiment and computer simulation for 18-beam case 21.98415 keV

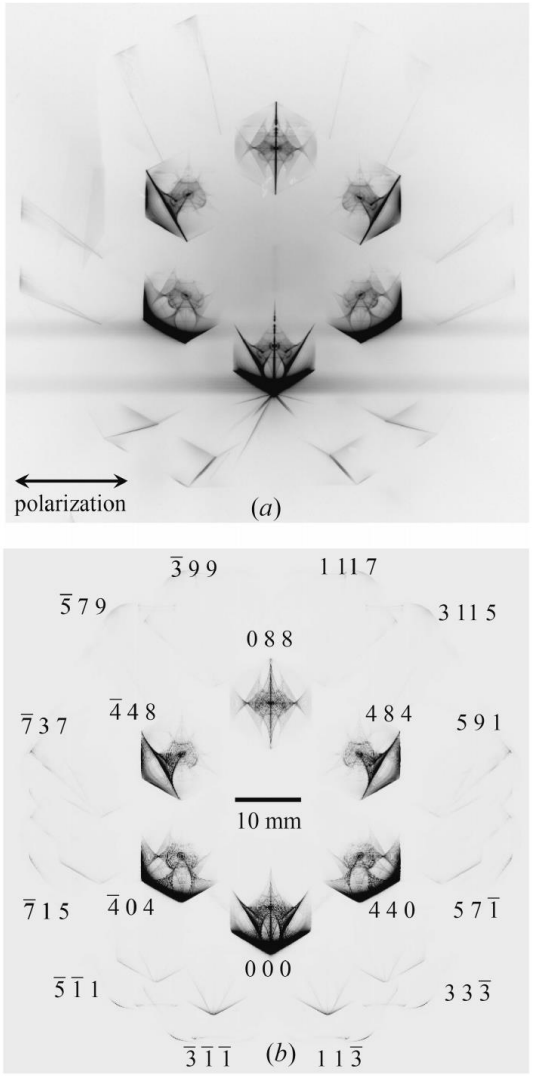

Fig. 18 (*a*) Experimentally obtained and (*b*) E-L&FFT simulated 18-beam pinhole topographs. (*b*) was obtained by the E-L &FFT simulation under an assumption of an incidence of X-rays with a photon energy $E = 21.98415$ keV ($\Delta E = E - E_0 = -0.25$ eV, where $E_0 = 21.98440$ keV) [reproduction of Fig. 3 in Okitsu *et al.* (2019)[40]].

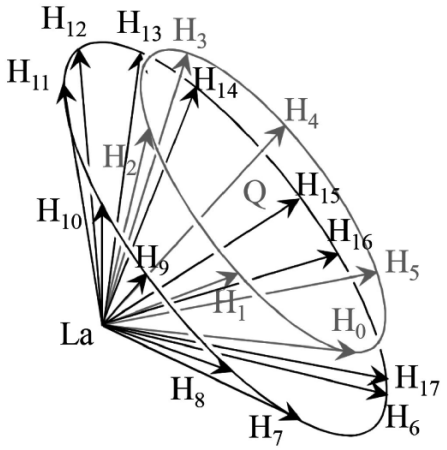

Fig. 19 (Color online) Six reciprocal lattice nodes are on a red (smaller) circle in reciprocal space. Outside of this circle, a black (larger) circle was observed on which twelve reciprocal lattice nodes were present. *Q* is the center of the red (smaller) circle [reproduction of Fig. 4 in Okitsu *et al.* (2019)[40]].

高木方程式とエバルト-ラウエ理論の等価性

2.2. Derivation of the *n*-beam Takagi-Taupin equation from the Ewald-Laue theory

In this section, the *n*-beam theory of T-T formulation is derived by Fourier-transforming the *n*-beam E-L theory described by (3).

2.3. Derivation of the *n*-beam E-L dynamical theory from the T-T equation

In this section, it is described that the *n*-beam E-L theory given by (3) can be derived from the *n*-beam T-T equation (14).

体系化した
議論が必要

高木方程式
(1962)

エバルト-ラウエ理論
(1917-1931)

31年

多波ケースの解法
(沖津2003)

フーリエ変換

多波ケースの解法
(Colella1974)

41年

39年

43年

シュレディンガー
方程式(1926)

2年

ハイゼンベルグ理論
(1924)

微分方程式

シュレディンガー
&ディラック

行列の固有値問題

18